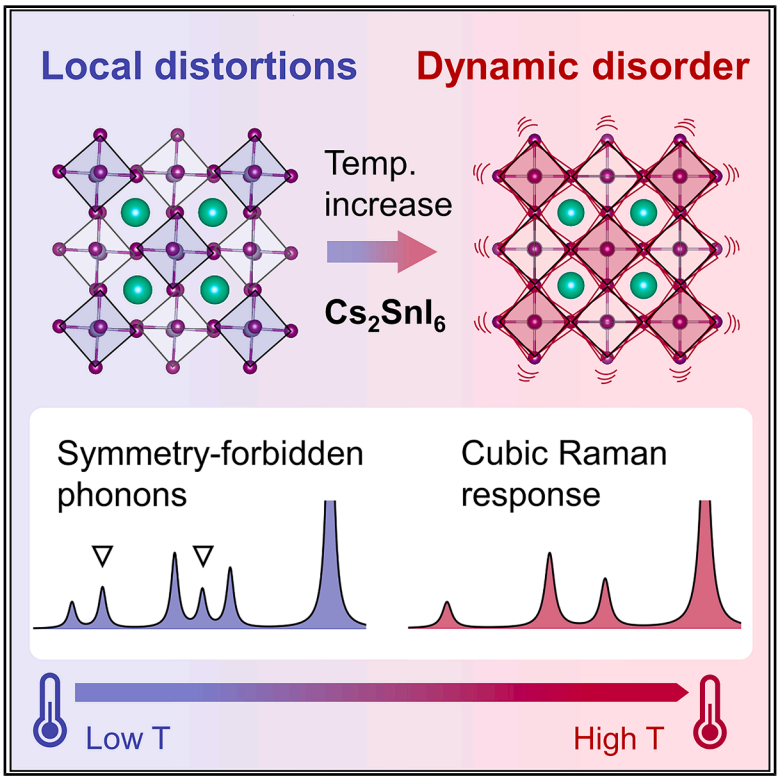
Newton

Article

Temperature-dependent Raman signatures of local symmetry breaking in vacancy-ordered double perovskite Cs_2SnI_6

Graphical abstract



Highlights

- Raman spectroscopy and DFT reveal local symmetry breaking in cubic Cs_2SnI_6
- Symmetry-forbidden phonons emerge below approximately 200 K
- Phonon intensities share a thermally activated energy scale of 15–20 meV
- Enhanced multi-phonon scattering signals strong electron-phonon coupling

Authors

Tomke E. Glier, Nicholas J. Weadock, Julian A. Vigil, ..., Volker Blum, Michael F. Toney, Dmitry Reznik

Correspondence

tomke.glier@uni-hamburg.de (T.E.G.), dmitry.reznik@colorado.edu (D.R.)

In brief

Despite their apparent symmetry, halide perovskites can host hidden distortions that affect their properties. Using temperature-dependent Raman spectroscopy and first-principles calculations, Glier et al. observed that symmetry-forbidden phonons emerged in the vacancy-ordered double perovskite Cs_2SnI_6 at low temperatures, despite the persistence of the average cubic structure. A common activation energy of 15–20 meV characterizes the temperature-dependent Raman response, while enhanced multi-phonon scattering highlights strong electron-phonon coupling, demonstrating Raman spectroscopy as a sensitive probe of hidden local structural behavior.

Glier et al., 2027, Newton *3*, 100724
March 1, 2027 © 2026 The Author(s). Published by Elsevier Inc.
https://doi.org/10.1016/j.newton.2026.100724

CellPress

Please cite this article in press as: Glier et al., Temperature-dependent Raman signatures of local symmetry breaking in vacancy-ordered double perovskite Cs_2SnI_6, Newton (2026), https://doi.org/10.1016/j.newton.2026.100724

Newton

CellPress
OPEN ACCESS

Article

Temperature-dependent Raman signatures of local symmetry breaking in vacancy-ordered double perovskite Cs_2SnI_6

Tomke E. Glier,[1,9,10,*] Nicholas J. Weadock,[2] Julian A. Vigil,[3] Cole Shank,[1] Xixi Qin,[4,5] Gabriel J. Graf,[4] Hemamala I. Karunadasa,[3,6] Volker Blum,[4,7] Michael F. Toney,[8] and Dmitry Reznik[1,*]

[1]Department of Physics, University of Colorado Boulder, Boulder, CO 80309, USA
[2]Materials Science and Engineering Program, University of Colorado Boulder, Boulder, CO 80303, USA
[3]Department of Chemistry, Stanford University, Stanford, CA 94305, USA
[4]Thomas Lord Department of Mechanical Engineering and Materials Science, Duke University, Durham, NC 27708, USA
[5]SLAC National Accelerator Laboratory, Menlo Park, CA, USA
[6]Stanford Institute for Materials and Energy Sciences, SLAC National Accelerator Laboratory, Menlo Park, CA 94025, USA
[7]Department of Chemistry, Duke University, Durham, NC 27708, USA
[8]Materials Science and Engineering Program, Department of Chemical and Biological Engineering, Renewable and Sustainable Energy Institute, University of Colorado Boulder, Boulder, CO 80309, USA
[9]Present address: Institute of Nanostructure and Solid State Physics, University of Hamburg, 22761 Hamburg, Germany
[10]Lead contact
*Correspondence: tomke.glier@uni-hamburg.de (T.E.G.), dmitry.reznik@colorado.edu (D.R.)
https://doi.org/10.1016/j.newton.2026.100724

ACCESSIBLE OVERVIEW Materials can appear highly symmetric when viewed on long length scales while still hosting local distortions that strongly influence their physical properties. Detecting such hidden structural organization is particularly important in halide perovskites, whose soft and anharmonic lattices give rise to complex structural dynamics and strong interactions between electronic excitations and atomic vibrations. Distinguishing these local effects from conventional structural phase transitions, however, remains challenging. Here, we use temperature-dependent Raman spectroscopy, together with first-principles calculations, to investigate the vacancy-ordered halide perovskite Cs_2SnI_6. Although its average crystal structure remains cubic down to cryogenic temperatures, additional phonons become Raman-active on cooling, thus revealing a local breakdown of the selection rules expected for the ideal cubic structure. Calculations for a relaxed lower-symmetry structure are consistent with this interpretation. The temperature evolution of the Raman response is governed by a common energy scale of 15–20 meV, while enhanced multi-phonon scattering under near-resonant excitation points to strong electron-phonon coupling. These results illustrate how local lattice distortions and their dynamics can remain hidden within an apparently high-symmetry crystal structure. More broadly, they demonstrate how Raman spectroscopy can reveal local structural organization that is hidden from probes of the average crystal structure and provide a framework for studying the interplay of local symmetry, anharmonicity, and electron-phonon coupling in vacancy-ordered halide perovskites.

SUMMARY

Understanding and controlling the optical, thermal, and mechanical properties of K_2PtCl_6-type double perovskites, commonly known as vacancy-ordered double perovskites, is essential for designing lead-free, high-performance thermoelectric and optoelectronic materials. We investigate Cs_2SnI_6 using temperature-dependent near-resonance Raman scattering, complemented by density-functional-theory-based phonon calculations. The appearance of Raman-forbidden phonon modes at cryogenic temperatures provides strong evidence for local symmetry breaking that does not develop into a global structural phase transition. Through detailed analysis of Raman intensities, energies, and line shapes, we characterize the temperature evolution of the symmetry-broken structural response of Cs_2SnI_6. Below 200 K, multi-phonon scattering is strongly enhanced, and symmetry-forbidden Raman modes emerge. The temperature dependence of Raman mode

This is an open access article under the CC BY-NC-ND license (http://creativecommons.org/licenses/by-nc-nd/4.0/).

Please cite this article in press as: Glier et al., Temperature-dependent Raman signatures of local symmetry breaking in vacancy-ordered double perovskite Cs_2SnI_6, Newton (2026), https://doi.org/10.1016/j.newton.2026.100724

intensities follows a phenomenological Arrhenius behavior, revealing an activation energy of 15–20 meV. These results establish temperature-dependent Raman spectroscopy as a sensitive probe of local structural distortions and anharmonic dynamics in Cs_2SnI_6, and they provide insight into local symmetry breaking and electron-phonon coupling in halide double perovskites.

INTRODUCTION

Metal-halide perovskites (ABX_3, X = halide) have emerged as exceptional optoelectronic materials, noted for their long carrier lifetimes, high defect tolerance, and strong light-matter interactions. These properties are commonly associated with their soft and polar structures, in which electronic excitations are strongly coupled to atomic vibrations.[1–4] In lead-halide perovskites, the mechanically soft structure (particularly the corner-sharing metal-halide octahedral framework) can deform around photogenerated electrons and holes, enabling the formation of large polarons that extend over several unit cells.[3,5,6] This strong electron-phonon coupling leads to effective structure-driven screening that shields charge carriers from scattering and trapping,[7] and local polar fluctuations have been shown to be intrinsic to the metal-halide perovskite lattice, independent of whether the A-site cation is organic or inorganic.[3,8,9] Raman spectroscopy has played a key role in establishing this picture, as low-frequency Raman modes in lead-halide perovskites reveal pronounced polar fluctuations of the inorganic substructure that intensify at elevated temperatures and correlate with polaronic behavior.[8–10]

Cesium tin(IV) iodide (Cs_2SnI_6) is a lead-free double perovskite ($A_2BB'X_6$[11]) that has attracted attention for optoelectronics and energy-conversion applications, including photovoltaics and photodetectors.[12–15] Cs_2SnI_6 is a native n-type semiconductor with a direct optical band gap of $\sim$ 1.3 eV at room temperature.[12,16–18] In contrast to the tin(II) single-perovskite analogue $CsSnI_3$, Cs_2SnI_6 adopts the K_2PtCl_6-type perovskite structure,[19] in which half of the single-perovskite B-site positions are vacant. This structural motif leads to spatially isolated $[SnI_6]^{2-}$ octahedra, which strongly influences the thermodynamic stability, electronic behavior, and structural dynamics, while maintaining a globally cubic ($Fm\bar{3}m$) average structure.[20,21]

Unlike their ABX_3 counterparts, which typically undergo symmetry-lowering structural transitions below room temperature, many K_2PtCl_6-type double perovskites such as Cs_2SnI_6 retain this cubic structure down to cryogenic temperatures.[16] This structural robustness is accompanied by exceptionally low thermal conductivity, tunable band gaps within the optical spectral range, and enhanced air and moisture stability.[12,16,18,21–23] The characteristic structural dynamics are governed by a 2-fold rattling mechanism of Cs^+ ions and $[SnI_6]^{2-}$ octahedra and pronounced electron-phonon coupling.[2,24–27] In Cs_2SnI_6, these rattling modes contribute to strong lattice anharmonicity and enhanced phonon-phonon scattering.[28,29] Despite growing theoretical interest in electron-phonon coupling and polaron-related effects in vacancy-ordered double perovskites, experimental access to the associated structural distortions remains challenging. Diffraction-based techniques primarily probe average crystal structures and are inherently insensitive to short-range static or dynamic local distortions.[30–32] As a result, experimental signatures of local symmetry breaking may remain hidden even when such distortions play an important role in the structural and electronic response.

Raman spectroscopy offers a powerful and complementary approach to this problem. As a symmetry-sensitive probe governed by well-defined selection rules, Raman scattering provides direct access to atomic vibrations and their coupling to electronic excitations. In particular, the appearance of symmetry-forbidden Raman modes or enhanced multi-phonon scattering can serve as sensitive indicators of local structural distortions and strong electron-phonon interactions.[33,34]

In this work, we employ temperature-dependent, near-resonant Raman spectroscopy to investigate the structural dynamics of single-crystalline Cs_2SnI_6. We observe clear signatures of local symmetry reduction in the vibrational response, manifested by the activation of Raman modes that are symmetry-forbidden in the cubic structure and by a strong enhancement of multi-phonon scattering. By systematically tracking the energies, linewidths, and intensities of these modes as a function of temperature, we characterize the temperature-dependent behavior of the symmetry-broken structural response.

RESULTS

Symmetry-forbidden Raman modes and first-principles calculations

A_2SnI_6 perovskites consist of isolated $[SnI_6]^{2-}$ octahedra and lack Sn–I–Sn bridges. As a result, Raman-active modes are dominated by internal octahedral vibrations (Sn–I stretching and bending), while low-frequency phonon modes are less prominent than in $ASnI_3$, where corner-sharing octahedra enable strong Sn–I–Sn vibrational coupling.[24,35,36] Additionally, the high symmetry cubic structures typical of A_2BX_6 compounds impose stricter Raman selection rules, resulting in fewer observable Raman-active modes.[37]

Figure 1 shows representative Stokes Raman spectra of Cs_2SnI_6 acquired at 295 K (Figure 1A) and 6 K (Figure 1B) in parallel and crossed polarization. All spectra are corrected for the thermal population factor (Bose correction). At 295 K, the Raman response is dominated by the four first-order modes expected for the cubic $Fm\bar{3}m$ structure and commonly reported for Cs_2SnI_6.[36,38,39] Specifically, we observe the triply degenerate low-frequency $\nu^L(T_{2g})$ mode near 39 cm^{-1}, the $\delta(T_{2g})$ mode near 76 cm^{-1}, and the $\nu(E_g)$ and $\nu(A_{1g})$ stretching modes at approximately 96 and 132 cm^{-1}, respectively. In addition, a second-order feature assigned to $2\nu(A_{1g})$ is visible near 260 cm^{-1}. The comparison of parallel and crossed polarization confirms the expected selection rules for scattering from the (111) facet (Table 1 and Figure S4).[40]

Upon cooling, the Raman spectra evolve markedly: the overall phonon spectral weight increases and additional features emerge, yielding a substantially richer low-temperature

Please cite this article in press as: Glier et al., Temperature-dependent Raman signatures of local symmetry breaking in vacancy-ordered double perovskite Cs_2SnI_6, Newton (2026), https://doi.org/10.1016/j.newton.2026.100724

CellPress
OPEN ACCESS

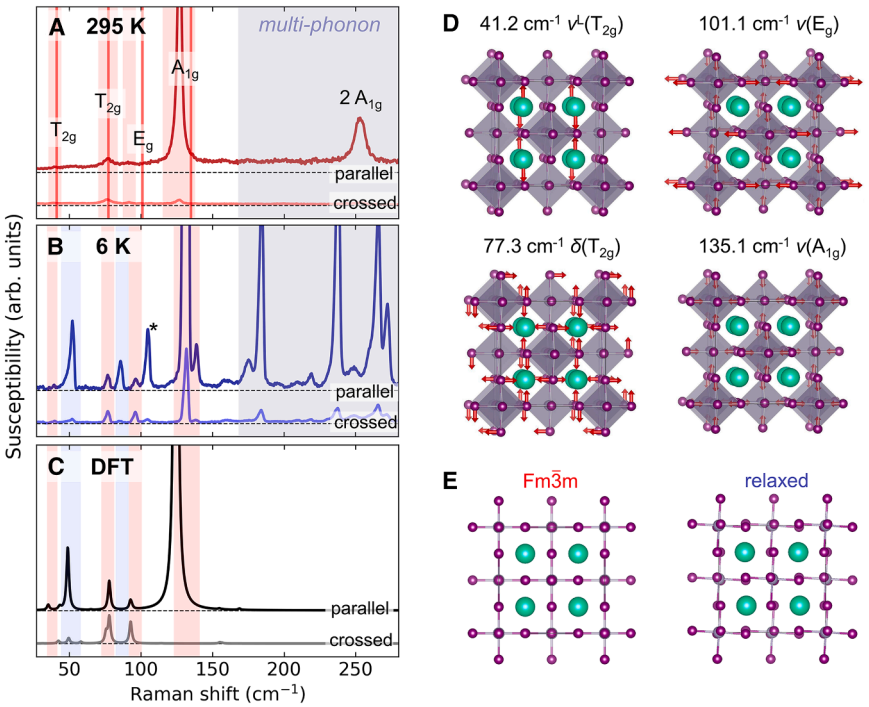


Figure 1. Cs_2SnI_6 Raman data

(A) Raman spectra at 295 K measured in $z(yy)\bar{z}$ (parallel, upper curve, $I_{\parallel}$) and $z(yx)\bar{z}$ (crossed, lower curve, $I_{\perp}$) polarization. Solid red vertical lines indicate the positions of the Raman-active phonons expected for the cubic $Fm\bar{3}m$ structure. Experimentally observed modes that can be assigned to these Raman-allowed phonons are highlighted in red, and their corresponding irreducible representations are indicated.

(B) Raman spectra at 6 K for $z(yy)\bar{z}$ (parallel, upper curve, $I_{\parallel}$) and $z(yx)\bar{z}$ (crossed, lower curve, $I_{\perp}$) polarization. Raman modes that emerge at cryogenic temperatures compared to room temperature are highlighted in blue. The star denotes a feature previously discussed as a combination mode.[38,41] Dashed horizontal lines in (A) and (B) indicate zero Raman susceptibility. In the gray shaded region, multi-phonon features are observed. All Raman spectra are corrected for the temperature-dependent Bose function.

(C) DFT-calculated Raman intensity for the relaxed structure obtained by relaxing and symmetrizing the atomic positions while fixing at the 100 K lattice constant, after initiating the symmetry-breaking relaxation by applying a small displacement along one of the three degenerate imaginary Γ-point phonon modes. Parallel and crossed scattering geometries have been calculated relative to the (111) facet matching the experimental conditions.

(D) Raman-active phonon modes and calculated Raman shifts corresponding to the experimental $Fm\bar{3}m$ crystal structure of Cs_2SnI_6. The Γ-point phonon energies and irreducible representations were obtained from finite-displacement DFT phonon calculations using a $1 \times 1 \times 1$ supercell of the conventional unit cell. Green, purple, and gray spheres represent Cs, I, and Sn atoms, respectively. Gray shaded polyhedra represent $[SnI_6]^{2-}$ octahedra. Red arrows indicate atomic displacement vectors associated with the phonon modes.

(E) Experimental $Fm\bar{3}m$ and relaxed structure for DFT. Green, purple, and gray spheres represent Cs, I, and Sn atoms, respectively. See methods for details.

spectrum (Figure 1B). Besides the first-order modes already present at 295 K (red), additional peaks appear below ~200 K, most prominently in the frequency range above ~170 cm^{-1}. Here, enhanced by near-resonant excitation, a dense set of multi-phonon features is observed. Consistent with previous reports, we also resolve a feature near 105 cm^{-1} that has been discussed as a combination mode.[38,41]

In addition to the enhanced multi-phonon response, new low-energy features become clearly visible at low temperature (shaded blue): a mode near 50 cm^{-1} with a strongly asymmetric lineshape and a mode near 86 cm^{-1}. Notably, these frequencies are close to the energies expected for infrared (IR)-active phonons of the ideal cubic $Fm\bar{3}m$ phase (Table S2). The appearance of intensity at the frequencies of nominally IR-active modes in a Raman experiment is consistent with a relaxation of the strict selection rules of the centrosymmetric high-symmetry structure. This is commonly associated with local symmetry reduction, which can render modes that are symmetry-forbidden in the ideal structure observable in the Raman response.[42] The calculated vibration patterns shown in Figure S7 confirm that the relevant T_{1u} and T_{2u} modes correspond to symmetric vibrational motions of the $[SnI_6]^{2-}$ octahedra that are Raman-inactive in ideal cubic O_h symmetry. Any local deviation from this centrosymmetric environment, such as bond-length variations or distortions of the octahedral units, can lift inversion symmetry and lower the local point group symmetry (e.g., to C_{2v} or C_{3v}). Under such reduced symmetry, the Raman selection rules are relaxed, and formerly Raman-inactive modes can acquire Raman activity, providing a natural explanation for the emergence of additional peaks near 50 and 86 cm^{-1}. At temperatures above 200 K, these additional low-energy features broaden and weaken, becoming increasingly difficult to distinguish from the background. At room temperature, they are no longer resolved, such that the investigated temperature range captures their evolution from well-defined low-temperature modes to their disappearance into the background. The near-resonant excitation conditions can enhance the Raman cross-section and thereby increase the visibility of weak spectral features. However, Cs_2SnI_6 exhibits a broad optical absorption onset rather than a discrete resonance near the excitation energy of 1.85 eV.[16] We therefore distinguish between resonance enhancement, which affects the detectability and intensity of the additional modes, and the relaxation of the first-order Raman selection rules, which we attribute to local symmetry reduction.

Figure 1C presents the density functional theory (DFT)-calculated Raman spectrum for the relaxed structure. This structure was obtained by relaxing the atomic positions at the fixed 100 K lattice constant after applying a small displacement along one of the three degenerate imaginary Γ-point phonon modes (see methods and Figure 1E). The resulting structure was found to exhibit $P2_1/c$ symmetry with a small numerical tolerance, and the atomic positions were refined accordingly, resulting in a negligible total energy change. The final structure and the

Table 1. Experimentally observed Raman-active single-phonon modes of Cs_2SnI_6 along with theoretically calculated modes for the experimental cubic $Fm\bar{3}m$ structure

	Theory		Experiment (6 K)	
	Raman shift	$I_\perp/I_\parallel$	Raman shift	$I_\perp/I_\parallel$
T_{2g}	41.2 cm^{-1}	2/3	39 cm^{-1}	0.69 ± 0.11
T_{2g}	77.3 cm^{-1}	2/3	76 cm^{-1}	0.74 ± 0.09
E_g	101.1 cm^{-1}	1	96 cm^{-1}	1.04 ± 0.05
A_{1g}	135.1 cm^{-1}	0	132 cm^{-1}	0.042 ± 0.04

Raman intensity ratios of crossed vs. parallel polarization for scattering from the (111) crystal facet are denoted as $I_\perp/I_\parallel$ (see also Figure S4). Experimental Raman shifts are given for the measurements taken at 6 K. The polarization-dependent detection efficiency of the Raman setup was independently calibrated using a Si(111) reference crystal (see Figure S5).

corresponding Brillouin zone are shown in Figure S8. No remaining physically meaningful instabilities are observed in the phonon dispersion of this derivative structure (see Figure S9). Thus, this procedure captures the dominant structural instability predicted by the phonon calculations and provides a representative local distortion pattern. The Raman tensors were evaluated for the parallel and crossed scattering geometries relative to the (111) facet, matching the experimental configurations. The calculated Raman spectrum was constructed by applying Lorentzian lineshapes with a phonon broadening of Γ = 3 cm^{-1} to the DFT-derived mode frequencies and intensities. The relaxed structure reproduces the main experimental features observed at 6 K in good agreement, including the mode near 50 cm^{-1}. The calculated Raman intensities were rescaled by mode-dependent prefactors for comparison with experiment. Quantitative agreement of absolute intensities is not expected, as the DFT calculations do not include resonance Raman contributions present under the experimental excitation conditions. All calculated Γ-point mode frequencies and irreducible representations for the relaxed structure are presented in Table S3.

Temperature dependence of Raman-active phonons

Figure 2 summarizes the experimental temperature dependence of the four Raman-active single-phonon modes of the cubic $Fm\bar{3}m$ structure. The interpolated color plots in the low-frequency range in Figures 2A and 2B illustrate the evolution of the Raman response in crossed and parallel polarization over the full temperature range. Selected Raman spectra in crossed polarization are shown in Figure 2C. The Bose-corrected Raman spectra are fitted using Voigt profiles for the phonons and a tanh function as background (see Note S1) to account for the nature of all Raman response functions that tend to 0 for $\omega \to 0$. For the Voigt profiles, the Gaussian contribution represents the instrumental response function, which is determined by measuring the elastic laser line.

Figure 2D shows the temperature dependence of the integrated Raman susceptibility of the four Raman-active modes, normalized to their respective low-temperature values. Triangles for the $\nu(A_{1g})$ mode represent results from parallel polarization corresponding to the A_{1g} character. Circles are used for crossed polarization. For all modes, the integrated intensity decreases strongly with increasing temperature. The effect is particularly pronounced for the $\nu(A_{1g})$ and $\nu(E_g)$ modes, whose spectral weight is reduced by more than an order of magnitude between 6 and 295 K, whereas the low-energy T_{2g} modes exhibit a more moderate reduction.

Because the measurements were performed under near-resonant excitation, temperature-dependent changes in the resonance condition may contribute to the observed variation of the Raman intensities. Temperature-dependent optical studies of Cs_2SnI_6, however, report a gradual shift of the optical transition energy of only a few tens of meV over a comparable temperature range,[17,44] while the excitation energy of 1.85 eV remains well above the optical gap. We therefore expect changes in resonance enhancement to provide a comparatively minor contribution to the pronounced temperature dependence of the Raman spectral weight, although such effects cannot be fully excluded.

We find that the temperature dependence of the Raman spectral weight can be described phenomenologically by an Arrhenius-type expression[45–47]:

$$I_{Arr}(T) = \frac{I_0}{1+A\cdot \exp\left(-E_A/(k_B T)\right)} \qquad \text{(Equation 1)}$$

where E_A represents an activation energy, I_0 is the phonon susceptibility integral at T = 0, and A is a rate parameter. The fits yield an activation energy of E_A = 20 ± 3 meV together with the rate parameter A = 33 ± 0.5 for E_g and A_{1g} modes (96 and 132 cm^{-1}) and A = 6 ± 1 for the T_{2g} modes (39 and 77 cm^{-1}).

The temperature-dependent phonon frequencies extracted from Voigt fits are displayed in Figure 2E. The higher-energy stretching modes, $\nu(E_g)$ and $\nu(A_{1g})$, exhibit a pronounced softening with increasing temperature, amounting to a total shift of approximately 5 cm^{-1} between 6 and 295 K. In contrast, the two low-energy T_{2g} modes show only minimal frequency changes over the same temperature range.

The linewidths (full width at half maximum [FWHM]) obtained from the Lorentzian component of the Voigt profiles are plotted in Figure 2F. For all modes, the linewidth increases with temperature, reflecting enhanced phonon scattering at elevated temperatures. To provide a quantitative description of the temperature evolution of phonon frequencies and linewidths, we compare the data to the Klemens model for anharmonic phonon decay, which describes the symmetric decay of an optical phonon into two acoustic phonons.[43] Within this framework, the temperature dependences of phonon frequency $\omega(T)$ and width $\Gamma(T)$ can be approximated by

$$\omega(T) = \omega_0 - \frac{a}{\exp\left(\frac{\hbar\omega_0}{2k_B T}\right) - 1}, \qquad \text{(Equation 2)}$$

$$\Gamma(T) = \Gamma_0 + \frac{b}{\exp\left(\frac{\hbar\omega_0}{2k_B T}\right) - 1}, \qquad \text{(Equation 3)}$$

where ω_0 is the phonon frequency at T = 0 K, Γ_0 represents the FWHM at 0 K, and a and b correspond to phonon characteristic decay constants that contain the transition matrix element and

Please cite this article in press as: Glier et al., Temperature-dependent Raman signatures of local symmetry breaking in vacancy-ordered double perovskite Cs_2SnI_6, Newton (2026), https://doi.org/10.1016/j.newton.2026.100724

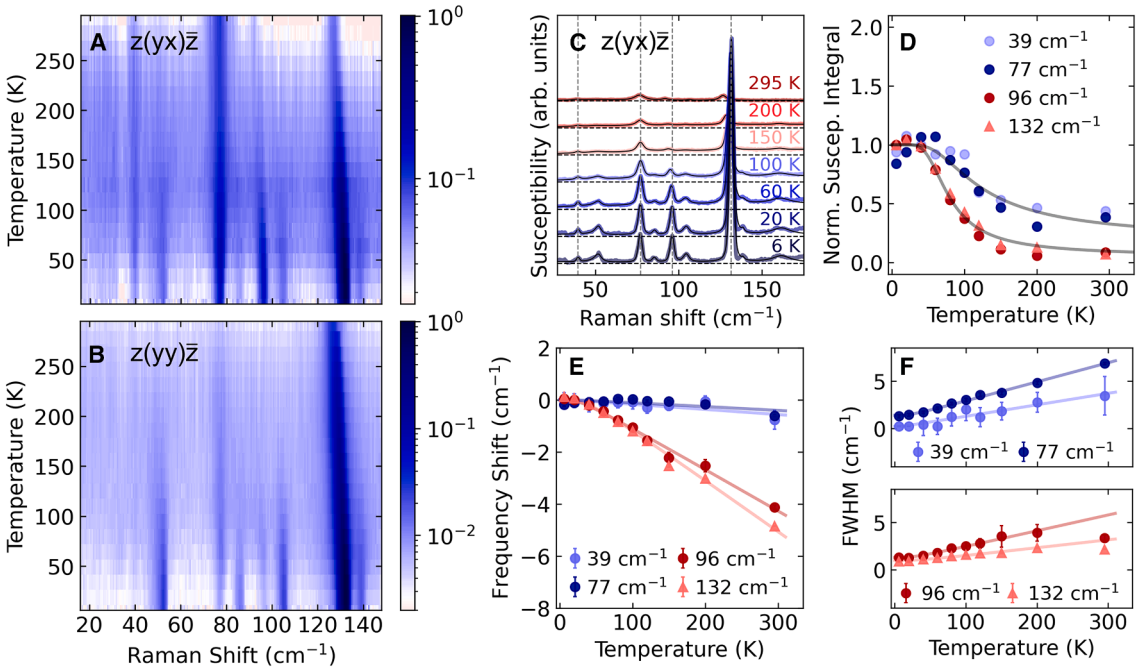


Figure 2. Raman susceptibility as a function of temperature

(A) Interpolated 2D color plot for crossed polarization. The colorbar represents the measured Raman intensity corrected for the temperature-dependent Bose function.

(B) Interpolated 2D color plot for parallel polarization. The colorbar represents the measured Raman intensity corrected for the temperature-dependent Bose function.

(C) Exemplary Raman spectra between 27 and 175 cm^{-1}. Raman spectra are corrected for the temperature-dependent Bose function. Dotted lines serve as guides to the eye, indicating the Raman mode frequencies measured at 6 K. The full dataset for $z(yx)\bar{z}$ and $z(yy)\bar{z}$ polarization is shown in Figure S1.

(D) Normalized phonon susceptibility integral extracted from the Raman fits. The curves are normalized to the respective susceptibility integral value at 6 K.

(E) Relative phonon frequency shift as a function of temperature for the four Raman-active phonon modes of the $Fm\bar{3}m$ structure (see Figure 1).

(F) Phonon full width at half maximum of the Lorentzian width determined by a Voigt fit.

Each data point in (E) and (F) was extracted from a fit to a Raman spectrum averaged over three consecutive acquisitions at the corresponding temperature and polarization configuration (n = 3 acquisitions). Error bars represent the standard errors of the fitted parameters obtained from the covariance matrices of the nonlinear least-squares fits to the averaged Raman spectra. The solid lines in (E) and (F) correspond to the Klemens model for a symmetric three-phonon anharmonic decay (see Equations 2 and 3).[43] In (D)–(F), the frequency, width, and integral of the A_{1g} mode are shown from parallel polarization (triangles), as this corresponds to the A_{1g} character. Circles represent crossed polarization. Phonon energies indicated in the legends correspond to experimental values measured at 6 K.

the two-phonon density of states of the anharmonic decay.[43,48,49] The model provides a phenomenological description of the observed softening and broadening of the $\nu(E_g)$ and $\nu(A_{1g})$ modes, while only very small decay constants are required to account for the nearly temperature-independent frequencies of the T_{2g} modes. All extracted fit parameters are summarized in Table S1.

Thermally activated Raman response and electron-phonon coupling

Taken together, the analysis of the symmetry-allowed Raman modes reveals two key aspects of the structural dynamics: (1) a pronounced and mode-dependent anharmonic softening and broadening and (2) a strong thermally activated reduction of phonon spectral weight characterized by an energy scale of approximately 15–20 meV. Importantly, this energy scale emerges consistently from the temperature dependence of all cubic Raman-active modes, suggesting that the observed behavior is not mode-specific but reflects a common underlying process.

Figure 3A schematically illustrates the crossover from locally symmetry-broken structural configurations at low temperatures (blue) to dynamically fluctuating disorder at elevated temperatures (red). This crossover is reflected in the Arrhenius-like temperature dependence of the Raman intensities. In this picture, the intensity of symmetry-forbidden modes serves as an indicator of the lifetime of locally distorted configurations. Figure 3D summarizes the temperature dependence of the integrated Raman susceptibility of the mode near 50 cm^{-1}, together with the Raman-active $\nu(A_{1g})$ and $\nu(E_g)$ modes. All three exhibit a similar reduction in spectral weight with increasing temperature. The 50 cm^{-1} mode follows an Arrhenius-type behavior (Equation 1) with an activation energy of 15 ± 3 meV, comparable to the energy scale extracted for the cubic Raman-active modes (Figure 2D). This common energy scale suggests that both symmetry-allowed and symmetry-forbidden features are influenced by a related thermally activated phonon process. Consistent with this picture, cooling enhances the Raman visibility of locally

Please cite this article in press as: Glier et al., Temperature-dependent Raman signatures of local symmetry breaking in vacancy-ordered double perovskite Cs_2SnI_6, Newton (2026), https://doi.org/10.1016/j.newton.2026.100724

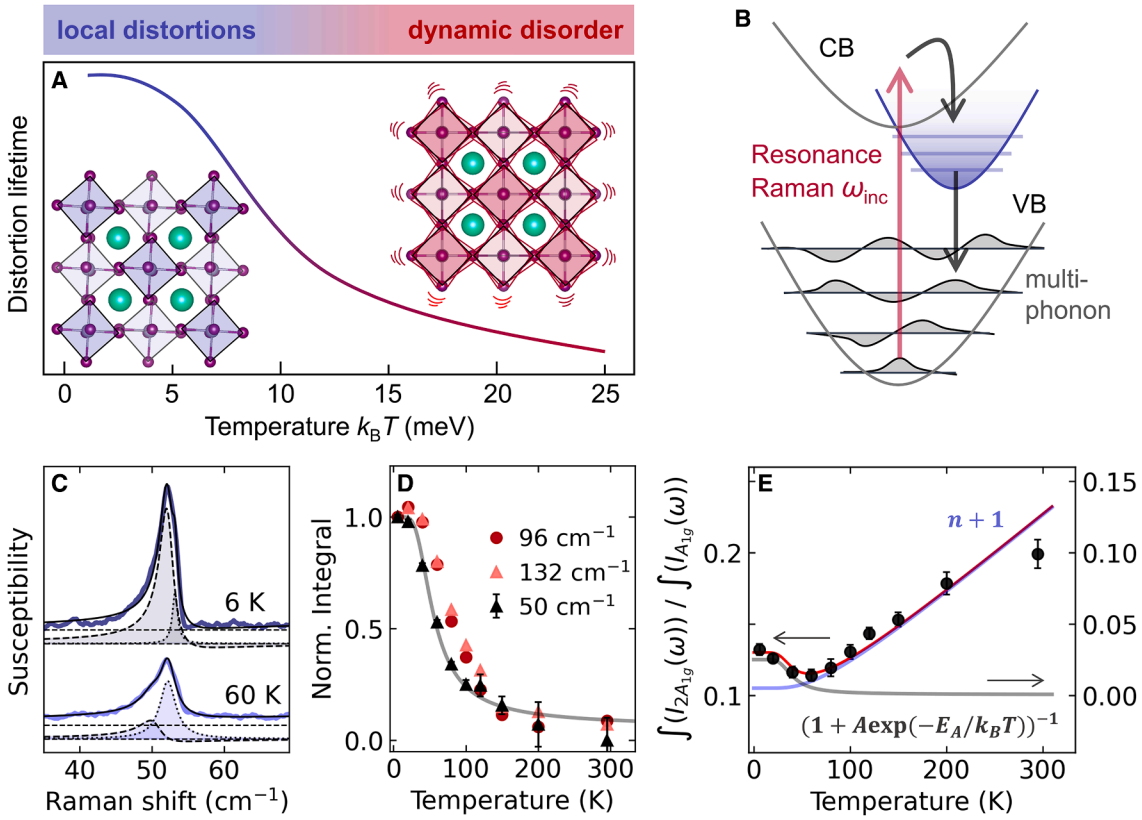


Figure 3. Interplay of local symmetry breaking and electron-phonon coupling

(A) Schematic illustration of the crossover from locally symmetry-broken/relaxed structural configurations at low temperatures to dynamically fluctuating disorder at elevated temperatures. The vertical axis represents the lifetime of locally distorted configurations as probed by Raman scattering. Upon increasing temperature, thermally activated structural fluctuations reduce the Raman visibility of local symmetry breaking.

(B) Franck-Condon-like representation of resonant Raman scattering. Under near-resonant excitation (ω_{inc}), strong electron-phonon coupling leads to a displacement of the excited-state potential surface along a configurational coordinate. A self-trapped state at low temperatures, illustrated in blue and displaced along the configurational coordinate, leads to enhanced multi-phonon scattering.

(C) IR-active phonon mode near 50 cm^{-1} at 6 and 60 K. The pronounced asymmetric lineshape is indicative of strong electron-phonon interactions. Fits to the data are shown as black solid lines. Lorentzian contribution is depicted as dotted line, Fano contribution is shown as dashed line. The shaded areas highlight the individual fit components for better visualization. Most importantly, the 60 K data yield a Fano parameter of $q = -2.6$, whereas the 6 K data exhibit a weaker Fano strength with $q = -5.5$, consistent with reduced coupling to the electronic continuum at low temperatures. The curves are offset for better visibility. Dashed horizontal lines mark zero.

(D) Normalized Raman susceptibility integral as a function of temperature for the T_{1u} mode shown in (C) (black). For comparison, data for the E_g and A_{1g} modes are also presented (red and light red, see also Figure 2D). The gray solid line represents the Arrhenius equation with an activation energy $E_A = 15$ meV.

(E) Integral ratio of two-phonon to single-phonon scattering intensity as a function of temperature for the A_{1g} mode. At temperatures above 100 K, the data follow the expected Bose ratio of $n + 1$ (blue solid line). At low temperatures, however, we observe an increased two-phonon Raman scattering intensity scaling with the localization of carriers in self-trapped states as fitted by the Arrhenius equation in Figure 3D and shown as gray solid line. The sum of blue and gray solid line is shown as red solid line.

Each data point in (D) and (E) was extracted from a fit to a Raman spectrum averaged over three consecutive acquisitions at the corresponding temperature and polarization configuration ($n = 3$ acquisitions). Error bars represent the standard errors of the fitted parameters obtained from the covariance matrices of the nonlinear least-squares fits to the averaged Raman spectra.

symmetry-reduced configurations, while increasing temperature restores the effective cubic response through rapid structural fluctuations.

Strong electron-phonon coupling in the soft and polar perovskite structure can promote carrier localization at low temperatures. Such localized (self-trapped) configurations, illustrated schematically in Figure 3B (blue potential), can influence the Raman response in two principal ways. First, changes in carrier localization can modify the effective polarizability response of the crystal structure, thereby affecting the overall Raman intensity.[46] Second, resonant-Raman scattering experiments revealed a significant enhancement of multi-phonon scattering under resonance conditions. Previous studies have reported multi-phonon scattering up to the 12th order when exciting above the optical band gap of halide perovskites.[50,51] This phenomenon can be explained using a Franck-Condon-like picture (Figure 3B), where strong electron-phonon interaction locally deforms the crystal structure

Please cite this article in press as: Glier et al., Temperature-dependent Raman signatures of local symmetry breaking in vacancy-ordered double perovskite Cs_2SnI_6, Newton (2026), https://doi.org/10.1016/j.newton.2026.100724

near a photoexcited carrier, leading to its self-trapping. Consequently, the excited electronic state possesses different atomic coordinates than the ground state when excited above the band gap.[52–54] As a result, we observe strong multi-phonon scattering as can be seen already in Figure 1. The temperature dependence of the ratio between the two-phonon overtone and the corresponding single-phonon $\nu(A_{1g})$ mode is shown in Figure 3E. At temperatures above approximately 100 K, the intensity ratio follows the expected Bose population factor $(n + 1)$. Upon further cooling, however, the ratio exceeds this expectation, indicating an additional low-temperature contribution to the multi-phonon Raman response. This excess component can be parametrized using the same Arrhenius-type expression, yielding an activation energy of approximately 15 meV, consistent with the energy scale extracted from the single-phonon analysis.

The low-energy feature near 50 cm^{-1} shows a pronounced asymmetric lineshape. Representative spectra at 6 and 60 K are shown in Figure 3C. The data can be well described by a superposition of a Lorentzian and a Fano profile, indicating strong electron-phonon coupling.[55] While the overall spectral weight of this mode increases upon cooling, the asymmetry of the lineshape is reduced at the lowest temperatures, as reflected by a change in the fitted Fano parameter from $q = -2.6$ at 60 K to $q = -5.5$ at 6 K.

DISCUSSION

The temperature-dependent Raman results presented here reveal a pronounced evolution of the vibrational response of Cs_2SnI_6 upon cooling, extending beyond the behavior expected for an ideal cubic structure. Three experimental observations are particularly salient: (1) a strong enhancement of phonon spectral weight at low temperatures, (2) the emergence of additional low-energy modes at cryogenic temperatures, and (3) a pronounced increase of multi-phonon scattering under near-resonant excitation conditions. A key observation is that both cubic-symmetry-allowed and cubic-symmetry-forbidden phonon modes share a common thermally activated intensity scale of 15–20 meV. This indicates that their temperature evolution is governed by a unified underlying process rather than mode-specific effects. Importantly, no experimental evidence for a *global* symmetry-lowering phase transition is found over the investigated temperature range, in agreement with diffraction studies reporting an average cubic structure down to cryogenic temperatures.[16] The Raman data, supported by the first-principles phonon calculations, therefore point to local, short-range symmetry reduction that does not develop into long-range structural order. This interpretation is consistent with previous total-scattering studies reporting local deviations from the ideal cubic structure despite the persistence of the cubic average structure.[28,56] These independent structural observations complement the symmetry-sensitive Raman response presented here.

The Raman-activation of the additional phonon modes can be understood within a unified framework that is consistent with both the experimental Raman data and first-principles calculations. DFT shows that a relaxed, symmetry-lowering structure derived from the cubic $Fm\bar{3}m$ phase naturally exhibits additional Raman-active modes at frequencies comparable to those observed experimentally (see Figure 1). This demonstrates that relatively modest deviations from the idealized high-symmetry average structure are sufficient to lift Raman selection rules and enrich the low-energy vibrational spectrum. From the experimental perspective, this is consistent with the local sensitivity of Raman scattering, which probes instantaneous or short-range structural configurations even when the average crystal structure remains cubic. Alternative origins of the additional low-energy features may include defect-induced Raman activity, disorder-induced relaxation of momentum conservation, or higher-order Raman processes. While such contributions cannot be excluded in general, several observations favor an assignment in terms of locally relaxed Raman selection rules. The modes near 50 and 86 cm^{-1} occur close to calculated zone-center phonons that are Raman-inactive in the ideal cubic structure and exhibit a systematic temperature evolution. Moreover, both features are reproducibly observed at spatially separated positions on the investigated crystal (Figure S6), arguing against an origin specific to a localized sample imperfection. Their frequencies can be accounted for by the calculated zone-center phonons without invoking disorder-induced sampling of phonons away from the Brillouin-zone center. A higher-order origin also appears less likely, as no comparably straightforward combination of the observed first-order Raman modes accounts for these features, whereas the pronounced multi-phonon Raman response occurs predominantly at higher Raman shifts. Taken together, we therefore consider local relaxation of the cubic Raman selection rules to provide the most consistent assignment of the additional low-energy modes.

Within this framework, one may envisage the following scenario. At elevated temperatures, the structure explores a broad manifold of locally distorted configurations[57] that average to the high-symmetry cubic structure, resulting in weak or strongly broadened signatures of symmetry-forbidden modes. Upon cooling, dynamic averaging over locally distorted configurations is progressively reduced, leading to longer-lived short-range distortions. This enhances the sensitivity of Raman scattering to local symmetry breaking and increases the visibility of modes that are inactive in the ideal structure. In this sense, the DFT-relaxed structure provides a useful static reference for the type of local symmetry breaking that can give rise to the observed additional phonon features, while the temperature dependence of the Raman intensities and lineshapes reflects the evolving contribution of these locally distorted configurations to the vibrational response.

The pronounced enhancement of multi-phonon scattering under near-resonant excitation further highlights the strong coupling between electronic excitations and atomic vibrations in this soft and anharmonic material. At elevated temperatures, the ratio of two-phonon to single-phonon scattering follows the expected Bose population behavior. At low temperatures, however, an additional contribution emerges that cannot be accounted for by population effects alone. Similar enhancements of higher-order Raman processes have been reported in other halide perovskites under resonant excitation and are commonly associated with strong electron-phonon

Please cite this article in press as: Glier et al., Temperature-dependent Raman signatures of local symmetry breaking in vacancy-ordered double perovskite Cs_2SnI_6, Newton (2026), https://doi.org/10.1016/j.newton.2026.100724

coupling.[50,51] In Cs_2SnI_6, the coexistence of strong multi-phonon scattering, the activation of symmetry-forbidden modes, and the pronounced temperature dependence of phonon spectral weight points to a highly anharmonic structure that is strongly coupled to electronic degrees of freedom.

In conclusion, the temperature-dependent Raman measurements reveal a pronounced evolution of the vibrational response of Cs_2SnI_6 upon cooling that cannot be fully described within the framework of a typical cubic structure. In addition to a strong enhancement of phonon spectral weight at low temperatures, cubic-symmetry-forbidden modes emerge and multi-phonon scattering becomes significantly enhanced under near-resonant excitation. The activation of modes near 50 and 86 cm^{-1}, at frequencies close to calculated zone-center phonons that are Raman-inactive in the ideal cubic phase, indicates a relaxation of Raman selection rules on local length scales. This interpretation is consistent with diffraction studies showing the persistence of the cubic average structure and with previous total-scattering studies reporting local structural deviations in Cs_2SnI_6.

First-principles calculations show that a relaxed, symmetry-lowering structure derived from the cubic phase naturally gives rise to additional Raman-active modes at comparable frequencies. The temperature dependence of both cubic-symmetry-allowed and cubic-symmetry-forbidden modes follows a common Arrhenius-type behavior with an energy scale of 15–20 meV, pointing to a shared thermally activated process governing the Raman visibility of locally distorted configurations. The simultaneous enhancement of multi-phonon scattering under near-resonant excitation further underscores the strong coupling between electronic excitations and lattice vibrations in this soft and anharmonic material. Together, these findings establish temperature-dependent Raman spectroscopy as a powerful probe of local symmetry breaking and electron-phonon interactions in vacancy-ordered halide perovskites.

METHODS

Raman measurements

We utilize a 671 nm (1.85 eV) CW laser source at a laser power of 2 mW and a spot size of the order of 100 μm. This laser energy is above the direct band gap of Cs_2SnI_6 of ~1.3 eV to take advantage of resonance-Raman effects. Due to the ultralow thermal conductivity of these materials, detailed laser power studies have been conducted to exclude sample damage or extreme laser heating (see Note S2 and Figures S2 and S3). The Raman instrument consists of a McPherson Scanning Monochromator (Model 207), equipped with a liquid-nitrogen cooled Pylon 100BRX (Teledyne) CCD detector. The Raman signal is collected in backscattering configuration. The elastic line is filtered by using three Bragg-Notch filters (Optigrate BNF-671-OD3-11M). The polarization-dependent detection efficiency of the Raman setup was independently calibrated using a Si(111) reference crystal (see Figure S5). Temperatures between 6 and 295 K were obtained by a Janis closed-cycle exchange-gas cryostat system. To assess the spatial reproducibility of the Raman response, low-temperature spectra were additionally recorded at two well-separated positions on the same Cs_2SnI_6 crystal under identical experimental conditions (Figure S6).

Preparation of Cs_2SnI_6 crystals

Millimeter-scale crystals of Cs_2SnI_6 were grown by slowly cooling (1–2°C h^{-1}) a saturated solution of the precursors in dry γ-butyrolactone from 130°C, as reported previously.[18] The Cs_2SnI_6 crystals were isolated from the mother liquor and stored in the dark in a dry atmosphere; crystals were cleaved with a blade prior to Raman measurements, revealing a fresh (111) termination.

Phonon and Raman calculations

All DFT calculations in this work were performed using the all-electron electronic structure code FHI-aims[58] with numeric atom-centered orbital (NAO) basis sets. Two structures were considered for the phonon calculations: the experimental structure with space group $Fm\bar{3}m$ measured at 100 K and a relaxed structure obtained by first applying a small displacement along one of the three degenerate imaginary Γ-point phonon modes of the 100 K experimental structure, followed by relaxation and symmetrization of the atomic positions while keeping the lattice constants fixed to the 100 K values. For the experimental structure, phonon calculations were performed using a $1 \times 1 \times 1$ supercell of the conventional unit cell (36 atoms) with atomic displacements of 0.005 Å. The resulting force constants were folded back to the primitive cell (9 atoms) to obtain phonon energies and irreducible representations of Γ-point modes. The relaxation was performed using the Perdew-Burke-Ernzerhof (PBE) exchange-correlation functional[59] with the Tkatchenko-Scheffler (TS) pairwise dispersion correction,[60] including the alkali modification introduced and benchmarked previously.[61] This level of theory has been shown to predict structures for metal-halide perovskites in close agreement with experiment in numerous past studies by our group.[62–64] FHI-aims' "intermediate" basis sets and other numerical defaults were employed, and the k-grid used was $4 \times 4 \times 4$. Structural relaxation was considered complete once the maximum residual force on every atomic coordinate was below 0.0001 eV/Å. The atomic positions were symmetrized, and the structure was brought to a primitive cell in the new space group (18 atoms) using pymatgen's spglib interface SpaceGroupAnalyzer.[65,66] Phonons were computed in a $3 \times 3 \times 2$ supercell of the primitive unit cell (324 atoms total) on a $2 \times 2 \times 2$ k-grid, and the force constants were folded back to the primitive cell. Structures with atomic displacements of 0.01 Å were generated using the Phonopy code,[67] and forces were calculated at the DFT-PBE+TS_alkali level of theory with the "intermediate" basis sets. Born effective charges (BECs) for non-analytical term correction (NAC) were calculated in the primitive cell using the same level of theory, basis sets, numerical settings, and a $6 \times 6 \times 4$ k-grid. The dynamical matrix was then constructed from the force-constant matrix and used to determine phonon frequencies and eigenvectors. Raman spectra for the relaxed structure were calculated using density-functional perturbation theory (DFPT),[68] by evaluating the finite-difference polarizability gradients in the primitive cell using the same basis sets, numerical settings, and a $6 \times 6 \times 4$ k-grid.

RESOURCE AVAILABILITY

Lead contact

Requests for further information and resources should be directed to and will be fulfilled by the lead contact, Tomke E. Glier (tomke.glier@uni-hamburg.de).

Materials availability

This study did not generate new materials.

Data and code availability

- All Raman data reported in this paper will be shared by the lead contact upon request. All computational structure optimizations, phonon calculations, and Raman intensity calculations can be obtained from the Duke Data Repository, DOI: https://doi.org/10.7924/r4r592. The atomic geometries for the cubic $Fm\bar{3}m$ structure used for initial phonon calculations and the computationally relaxed, lower-symmetry structure used for phonon and Raman intensity calculations are listed in Note S6. These structures, along with experimental Raman data at 6 and 295 K, can be found in the HybriD^3 database via https://materials.hybrid3.duke.edu/materials/search with dataset IDs 3045, 3044, 3076, and 3077, respectively.
- This paper does not report original code.
- Any additional information required to reanalyze the data reported in this paper is available from the lead contact upon request. Additional relevant data can be obtained from the corresponding author or the first author upon reasonable request.

ACKNOWLEDGMENTS

The authors thank Nathan R. Wolf (Stanford University) for support with measurements of the experimental Cs_2SnI_6 structure at 100 K. Aspects of the data interpretation (N.J.W. and M.F.T.) were supported by the Center for Hybrid Organic Inorganic Semiconductors for Energy, an Energy Frontier Research Center funded by the Office of Basic Energy Sciences, Office of Science within the US Department of Energy (DOE). J.A.V. acknowledges fellowship support from the Stanford University Office of the Vice Provost of Graduate Education and the National Science Foundation Graduate Research Fellowship Program under grant no. DGE-1656518. T.G. and D.R. were supported by the US Department of Energy, Office of Basic Energy Sciences, Office of Science, under contract no. DE-SC0024117. Apparatus customization and preliminary measurements conducted by C.S. were supported by the NSF grant No DMR-2210126. X.Q., G.J.G., and V.B. were supported by the National Science Foundation under award number 2323803 for the first-principles simulations included in this work. G.J.G. was also supported by the National Science Foundation under grant DGE-2022040 for computational data analysis and additional first-principles simulations included in this work. X.Q. acknowledges the computational resources provided by the National Energy Research Scientific Computing Center (NERSC), a US Department of Energy (DOE) Office of Science User Facility, operated under contract no. DE-AC02-05CH11231. G.J.G. acknowledges computational resources sponsored by the Department of Energy and located at the National Laboratory of the Rockies. H.I.K. acknowledges funding through the DOE Office of Basic Energy Sciences, Division of Materials Science and Engineering under contract no. DE-AC02-76SF00515 (sample preparation).

AUTHOR CONTRIBUTIONS

Conceptualization, T.E.G. and D.R.; methodology, T.E.G., D.R., V.B., X.Q., and G.J.G.; investigation, T.E.G., C.S., V.B., X.Q., and G.J.G.; formal analysis, T.E.G., V.B., X.Q., and G.J.G.; resources, J.A.V., N.J.W., and H.I.K.; writing – original draft, T.E.G. and D.R.; writing – review and editing, T.E.G., D.R., N.J.W., J.A.V., X.Q., G.J.G., V.B., and M.F.T.; visualization, T.E.G., X.Q., and G.J.G.; funding acquisition, D.R., H.I.K., M.F.T., and V.B.

DECLARATION OF INTERESTS

The authors declare no competing interests.

SUPPLEMENTAL INFORMATION

Supplemental information can be found online at https://doi.org/10.1016/j.newton.2026.100724.

Received: May 22, 2026
Revised: August 31, 2026
Accepted: October 9, 2026

REFERENCES

1. Puppin, M., Polishchuk, S., Colonna, N., Crepaldi, A., Dirin, D.N., Nazarenko, O., De Gennaro, R., Gatti, G., Roth, S., Barillot, T., et al. (2020). Evidence of large polarons in photoemission band mapping of the perovskite semiconductor $CsPbBr_3$. Phys. Rev. Lett. *124*, 206402. https://doi.org/10.1103/PhysRevLett.124.206402.
2. Yamada, Y., and Kanemitsu, Y. (2022). Electron-phonon interactions in halide perovskites. NPG Asia Mater. *14*, 48. https://doi.org/10.1038/s41427-022-00394-4.
3. Miyata, K., Meggiolaro, D., Trinh, M.T., Joshi, P.P., Mosconi, E., Jones, S.C., De Angelis, F., and Zhu, X.-Y. (2017). Large polarons in lead halide perovskites. Sci. Adv. *3*, e1701217. https://doi.org/10.1126/sciadv.1701217.
4. Ghosh, D., Welch, E., Neukirch, A.J., Zakhidov, A., and Tretiak, S. (2020). Polarons in halide perovskites: A perspective. J. Phys. Chem. Lett. *11*, 3271–3286. https://doi.org/10.1021/acs.jpclett.0c00018.
5. Munson, K.T., and Asbury, J.B. (2021). Influence of dynamic disorder and charge–lattice interactions on optoelectronic properties of halide perovskites. J. Phys. Chem. C *125*, 5427–5435. https://doi.org/10.1021/acs.jpcc.0c10889.
6. Guzelturk, B., Winkler, T., Van de Goor, T.W.J., Smith, M.D., Bourelle, S.A., Feldmann, S., Trigo, M., Teitelbaum, S.W., Steinrück, H.-G., de la Pena, G.A., et al. (2021). Visualization of dynamic polaronic strain fields in hybrid lead halide perovskites. Nat. Mater. *20*, 618–623. https://doi.org/10.1038/s41563-020-00865-5.
7. Jin, H., Debroye, E., Keshavarz, M., Scheblykin, I.G., Roeffaers, M.B.J., Hofkens, J., and Steele, J.A. (2020). It's a trap! on the nature of localised states and charge trapping in lead halide perovskites. Mater. Horiz. *7*, 397–410. https://doi.org/10.1039/C9MH00500E.
8. Yaffe, O., Guo, Y., Tan, L.Z., Egger, D.A., Hull, T., Stoumpos, C.C., Zheng, F., Heinz, T.F., Kronik, L., Kanatzidis, M.G., et al. (2017). Local polar fluctuations in lead halide perovskite crystals. Phys. Rev. Lett. *118*, 136001. https://doi.org/10.1103/PhysRevLett.118.136001.
9. Reuveni, G., Diskin-Posner, Y., Gehrmann, C., Godse, S., Gkikas, G.G., Buchine, I., Aharon, S., Korobko, R., Stoumpos, C.C., Egger, D.A., and Yaffe, O. (2023). Static and dynamic disorder in formamidinium lead bromide single crystals. J. Phys. Chem. Lett. *14*, 1288–1293. https://doi.org/10.1021/acs.jpclett.2c03337.
10. Miyata, K., Atallah, T.L., and Zhu, X.-Y. (2017). Lead halide perovskites: Crystal-liquid duality, phonon glass electron crystals, and large polaron formation. Sci. Adv. *3*, e1701469. https://doi.org/10.1126/sciadv.1701469.
11. Wolf, N.R., Connor, B.A., Slavney, A.H., and Karunadasa, H.I. (2021). Doubling the stakes: The promise of halide double perovskites. Angew. Chem. Int. Ed. Engl. *60*, 16264–16278. https://doi.org/10.1002/anie.202016185.
12. Lee, B., Stoumpos, C.C., Zhou, N., Hao, F., Malliakas, C., Yeh, C.-Y., Marks, T.J., Kanatzidis, M.G., and Chang, R.P.H. (2014). Air-stable molecular semiconducting iodosalts for solar cell applications: Cs_2SnI_6 as a hole conductor. J. Am. Chem. Soc. *136*, 15379–15385. https://doi.org/10.1021/ja508464w.
13. Ullah, S., Wang, J., Yang, P., Liu, L., khan, J., Yang, S.-E., Xia, T., Guo, H., and Chen, Y. (2021). Lead-free Cs_2SnI_6 perovskites for optoelectronic

applications: Recent developments and perspectives. Sol. RRL *5*, 2000830. https://doi.org/10.1002/solr.202000830.

14. Chauhan, A., Alla, M., Oudhia, A., Shrivastav, A., Elfatouaki, F., Alla, M., Fares, B., Narayana, B., and Sinha, A.K. (2025). Complete study to boosting the power conversion efficiency of inorganic double perovskite Cs_2SnI_6 non-toxic and stable with efficiency ≈23%. Renew. Energy *242*, 122425. https://doi.org/10.1016/j.renene.2025.122425.
15. Anil Kumar, A.E., Nair, S., and Thoutam, L.R. (2024). The prospects and challenges for ambi-polar vacancy-ordered double-perovskite Cs_2SnI_6 toward realization of high-efficiency air-stable solar-cells. Sol. RRL *8*, 2400275. https://doi.org/10.1002/solr.202400275.
16. Maughan, A.E., Ganose, A.M., Bordelon, M.M., Miller, E.M., Scanlon, D.O., and Neilson, J.R. (2016). Defect tolerance to intolerance in the vacancy-ordered double perovskite semiconductors Cs_2SnI_6 and Cs_2TeI_6. J. Am. Chem. Soc. *138*, 8453–8464. https://doi.org/10.1021/jacs.6b03207.
17. Luo, R., Zhang, S., Zhao, S., Li, J., Kang, F., Yu, K., and Wei, G. (2020). Ultrasmall blueshift of near-infrared fluorescence in phase-stable Cs_2SnI_6 thin films. Phys. Rev. Appl. *14*, 014048. https://doi.org/10.1103/PhysRevApplied.14.014048.
18. Vigil, J.A., Wolf, N.R., Slavney, A.H., Matheu, R., Saldivar Valdes, A., Breidenbach, A., Lee, Y.S., and Karunadasa, H.I. (2024). Halide perovskites breathe too: The iodide–iodine equilibrium and self-doping in Cs_2SnI_6. ACS Cent. Sci. *10*, 907–919. https://doi.org/10.1021/acscentsci.4c00056.
19. Werker, W. (1939). Die Krystallstruktur des Rb_2SnJ_6 und Cs_2SnJ_6. Recl. Trav. Chim. Pays-Bas *58*, 257–258. https://doi.org/10.1002/recl.19390580309.
20. Arunkumar, P., Cho, H.B., Gil, K.H., Unithrattil, S., Kim, Y.H., and Bin Im, W. (2018). Probing molecule-like isolated octahedra via phase stabilization of zero-dimensional cesium lead halide nanocrystals. Nat. Commun. *9*, 4691. https://doi.org/10.1038/s41467-018-07097-x.
21. Maughan, A.E., Ganose, A.M., Scanlon, D.O., and Neilson, J.R. (2019). Perspectives and design principles of vacancy-ordered double perovskite halide semiconductors. Chem. Mater. *31*, 1184–1195. https://doi.org/10.1021/acs.chemmater.8b05036.
22. Karim, M.M.S., Ganose, A.M., Pieters, L., Winnie Leung, W.W., Wade, J., Zhang, L., Scanlon, D.O., and Palgrave, R.G. (2019). Anion distribution, structural distortion, and symmetry-driven optical band gap bowing in mixed halide Cs_2SnX_6 vacancy ordered double perovskites. Chem. Mater. *31*, 9430–9444. https://doi.org/10.1021/acs.chemmater.9b03267.
23. Cai, Y., Xie, W., Ding, H., Chen, Y., Thirumal, K., Wong, L.H., Mathews, N., Mhaisalkar, S.G., Sherburne, M., and Asta, M. (2017). Computational study of halide perovskite-derived A_2BX_6 inorganic compounds: chemical trends in electronic structure and structural stability. Chem. Mater. *29*, 7740–7749. https://doi.org/10.1021/acs.chemmater.7b02013.
24. Jong, U.-G., Kim, Y.-S., Ri, C.-H., Kye, Y.-H., Pak, C.-J., Cottenier, S., and Yu, C.-J. (2022). Twofold rattling mode-induced ultralow thermal conductivity in vacancy-ordered double perovskite Cs_2SnI_6. Chem. Commun. *58*, 4223–4226. https://doi.org/10.1039/D2CC00258B.
25. Bhumla, P., Jain, M., Sheoran, S., and Bhattacharya, S. (2022). Vacancy-ordered double perovskites Cs_2BI_6 (B = Pt, Pd, Te, Sn): An emerging class of thermoelectric materials. J. Phys. Chem. Lett. *13*, 11655–11662. https://doi.org/10.1021/acs.jpclett.2c02852.
26. Wright, A.D., Verdi, C., Milot, R.L., Eperon, G.E., Pérez-Osorio, M.A., Snaith, H.J., Giustino, F., Johnston, M.B., and Herz, L.M. (2016). Electron–phonon coupling in hybrid lead halide perovskites. Nat. Commun. *7*, 0. https://doi.org/10.1038/ncomms11755.
27. Ghorui, S., Kangsabanik, J., Aslam, M., and Alam, A. (2024). Optoelectronic and transport properties of vacancy-ordered double-perovskite halides: A first-principles study. Phys. Rev. Appl. *21*, 024036. https://doi.org/10.1103/PhysRevApplied.21.024036.
28. Maughan, A.E., Paecklar, A.A., and Neilson, J.R. (2018). Bond valences and anharmonicity in vacancy-ordered double perovskite halides. J. Mater. Chem. C *6*, 12095–12104, URL:. https://doi.org/10.1039/C8TC03527J
29. Ghosh, M., Pal, P., Paul, T., Maiti, S., Bhattacharjee, S., Sardar, K., Sahoo, A., Ghosh, A., and Chattopadhyay, K.K. (2023). Charge-carrier dynamics and relaxation in Cs_2SnI_6 perovskite for energy storage: Existence of anharmonic rattling-assisted polaron dynamics. Phys. Rev. Appl. *20*, 054032. https://doi.org/10.1103/PhysRevApplied.20.054032.
30. Weadock, N.J., Sterling, T.C., Vigil, J.A., Gold-Parker, A., Smith, I.C., Ahammed, B., Krogstad, M.J., Ye, F., Voneshen, D., Gehring, P.M., et al. (2023). The nature of dynamic local order in $CH_3NH_3PbI_3$ and $CH_3NH_3PbBr_3$. Joule *7*, 1051–1066. https://doi.org/10.1016/j.joule.2023.03.017.
31. Beecher, A.N., Semonin, O.E., Skelton, J.M., Frost, J.M., Terban, M.W., Zhai, H., Alatas, A., Owen, J.S., Walsh, A., and Billinge, S.J.L. (2016). Direct observation of dynamic symmetry breaking above room temperature in methylammonium lead iodide perovskite. ACS Energy Lett. *1*, 880–887. https://doi.org/10.1021/acsenergylett.6b00381.
32. Liu, J., Phillips, A.E., Keen, D.A., and Dove, M.T. (2019). Thermal disorder and bond anharmonicity in Cesium lead iodide studied by neutron total scattering and the reverse Monte Carlo method. J. Phys. Chem. C *123*, 14934–14940. https://doi.org/10.1021/acs.jpcc.9b02936.
33. Saunders, C.N., Ladygin, V.V., Kim, D.S., Bernal-Choban, C.M., Lohaus, S.H., Granroth, G.E., Abernathy, D.L., and Fultz, B. (2025). Diffuse intensity from phonon noise in inelastic neutron scattering. Phys. Rev. Mater. *9*, 024602. https://doi.org/10.1103/PhysRevMaterials.9.024602.
34. Saunders, C.N., Kim, D.S., Hellman, O., Smith, H.L., Weadock, N.J., Omelchenko, S.T., Granroth, G.E., Bernal-Choban, C.M., Lohaus, S.H., Abernathy, D.L., and Fultz, B. (2022). Thermal expansion and phonon anharmonicity of cuprite studied by inelastic neutron scattering and ab initio calculations. Phys. Rev. B *105*, 174308. https://doi.org/10.1103/PhysRevB.105.174308.
35. Kontos, A.G., Kaltzoglou, A., Siranidi, E., Palles, D., Angeli, G.K., Arfanis, M.K., Psycharis, V., Raptis, Y.S., Kamitsos, E.I., Trikalitis, P.N., et al. (2017). Structural Stability, Vibrational Properties, and Photoluminescence in $CsSnI_3$ Perovskite upon the Addition of SnF_2. Inorg. Chem. *56*, 84–91. https://doi.org/10.1021/acs.inorgchem.6b02318.
36. Bhui, A., Ghosh, T., Pal, K., Singh Rana, K., Kundu, K., Soni, A., and Biswas, K. (2022). Intrinsically low thermal conductivity in the n-type vacancy-ordered double perovskite Cs_2SnI_6: Octahedral rotation and anharmonic rattling. Chem. Mater. *34*, 3301–3310. https://doi.org/10.1021/acs.chemmater.2c00084.
37. Rahim, W., Cheng, A., Lyu, C., Shi, T., Wang, Z., Scanlon, D.O., and Palgrave, R.G. (2020). Geometric analysis and formability of the cubic A_2BX_6 vacancy-ordered double perovskite structure. Chem. Mater. *32*, 9573–9583. https://doi.org/10.1021/acs.chemmater.0c02806.
38. Kaur, G., Shukla, A., Justice Babu, K., and Ghosh, H.N. (2022). Mapping the real-time vibrational infrastructure of Cs_2SnI_6 nanocrystals through coherent phonon dynamics. ACS Photonics *9*, 2756–2766. https://doi.org/10.1021/acsphotonics.2c00512.
39. Belessiotis, G., Arfanis, M., Kaltzoglou, A., Likodimos, V., Raptis, Y., Falaras, P., and Kontos, A. (2021). Temperature effects on the vibrational properties of the Cs_2SnX_6 'defect' perovskites (X = I, Br, Cl). Mater. Chem. Phys. *267*, 124679. https://doi.org/10.1016/j.matchemphys.2021.124679.
40. Cardona, M. (1982). In Light Scattering in Solids: Recent Results, M. Cardona and G. Güntherodt, eds. (Springer).
41. Folgueras, M.C., Jin, J., Gao, M., Quan, L.N., Steele, J.A., Srivastava, S., Ross, M.B., Zhang, R., Seeler, F., Schierle-Arndt, K., et al. (2021). Lattice dynamics and optoelectronic properties of vacancy-ordered double perovskite Cs_2TeX_6 ($X = Cl^-, Br^-, I^-$) single crystals. J. Phys. Chem. C *125*, 25126–25139. https://doi.org/10.1021/acs.jpcc.1c08332.
42. Lee, S., Kim, B.H., Seong, M.-J., and Choi, K.-Y. (2022). Noncubic local distortions and spin-orbit excitons in K_2IrCl_6. Phys. Rev. B *105*, 184433. https://doi.org/10.1103/PhysRevB.105.184433.

Please cite this article in press as: Glier et al., Temperature-dependent Raman signatures of local symmetry breaking in vacancy-ordered double perovskite Cs_2SnI_6, Newton (2026), https://doi.org/10.1016/j.newton.2026.100724

43. Klemens, P.G. (1966). Anharmonic decay of optical phonons. Phys. Rev. *148*, 845–848. https://doi.org/10.1103/PhysRev.148.845.

44. Belessiotis, G., Arfanis, M., Kaltzoglou, A., Likodimos, V., Raptis, Y., Falaras, P., and Kontos, A. (2022). Temperature dependence of the vibrational and emission spectra in the 0D vacancy-ordered Cs_2SnI_6 perovskite. Mater. Today Proc. *67*, 971–974. https://doi.org/10.1016/j.matpr.2022.07.260.

45. Soares, C.C.S., Rodríguez-Hernández, J.S., Gómez, M.A.P., Andrade, D.M., Fechine, P.B.A., Ayala, A.P., and Paschoal, C.W.A. (2024). Strong electron–phonon coupling in vacancy-ordered Cs_2SnBr_6 double perovskite. J. Mater. Chem. C *12*, 16758–16765. https://doi.org/10.1039/D4TC01818D.

46. McCall, K.M., Stoumpos, C.C., Kostina, S.S., Kanatzidis, M.G., and Wessels, B.W. (2017). Strong electron–phonon coupling and self-trapped excitons in the defect halide perovskites $A_3M_2I_9$ (A = Cs, Rb; M = Bi, Sb). Chem. Mater. *29*, 4129–4145. https://doi.org/10.1021/acs.chemmater.7b01184.

47. Rahane, S.N., Rahane, G.K., Mandal, A., Jadhav, Y., Godha, A., Rokade, A., Shah, S., Hase, Y., Waghmare, A., Saykar, N.G., et al. (2024). Lead-free $Cs_2AgBiCl_6$ double perovskite: Experimental and theoretical insights into the self-trapping for optoelectronic applications. ACS Phys. Chem. Au *4*, 476–489. https://doi.org/10.1021/acsphyschemau.4c00008.

48. Menéndez, J., and Cardona, M. (1984). Temperature dependence of the first-order Raman scattering by phonons in Si, Ge, and α-Sn: Anharmonic effects. Phys. Rev. B *29*, 2051–2059. https://doi.org/10.1103/PhysRevB.29.2051.

49. Buchenau, S., Scheitz, S., Sethi, A., Slimak, J.E., Glier, T.E., Das, P.K., Dankwort, T., Akinsinde, L., Kienle, L., Rusydi, A., et al. (2020). Temperature and magnetic field dependent Raman study of electron-phonon interactions in thin films of Bi_2Se_3 and Bi_2Te_3 nanoflakes. Phys. Rev. B *101*, 245431. https://doi.org/10.1103/PhysRevB.101.245431.

50. Iaru, C.M., Brodu, A., van Hoof, N.J.J., ter Huurne, S.E.T., Buhot, J., Montanarella, F., Buhbut, S., Christianen, P.C.M., Vanmaekelbergh, D., de Mello Donega, C., et al. (2021). Fröhlich interaction dominated by a single phonon mode in $CsPbBr_3$. Nat. Commun. *12*, 5844. https://doi.org/10.1038/s41467-021-26192-0.

51. Xu, K.-X., Lai, J.-M., Gao, Y.-F., Song, F., Sun, Y.-J., Tan, P.-H., and Zhang, J. (2022). High-order Raman scattering mediated by self-trapped exciton in halide double perovskite. Phys. Rev. B *106*, 085205. https://doi.org/10.1103/PhysRevB.106.085205.

52. Perebeinos, V., and Allen, P.B. (2001). Multiphonon resonant Raman scattering predicted in $LaMnO_3$ from the Franck-Condon process via self-trapped excitons. Phys. Rev. B *64*, 085118. https://doi.org/10.1103/PhysRevB.64.085118.

53. Krüger, R., Schulz, B., Naler, S., Rauer, R., Budelmann, D., Bäckström, J., Kim, K.H., Cheong, S.-W., Perebeinos, V., and Rübhausen, M. (2004). Orbital ordering in $LaMnO_3$ Investigated by Resonance Raman Spectroscopy. Phys. Rev. Lett. *92*, 097203. https://doi.org/10.1103/PhysRevLett.92.097203.

54. Andreasson, J., Holmlund, J., Knee, C.S., Käll, M., Börjesson, L., Naler, S., Bäckström, J., Rübhausen, M., Azad, A.K., and Eriksson, S.-G. (2007). Franck-Condon higher order lattice excitations in the $LaFe_{1-x}Cr_xO_3$ (x=0, 0.1, 0.5, 0.9, 1.0) perovskites due to Fe-Cr charge transfer effects. Phys. Rev. B *75*, 104302. https://doi.org/10.1103/PhysRevB.75.104302.

55. Klein, M.V. (1983). Electronic Raman Scattering (Springer Berlin Heidelberg), pp. 147–204. https://doi.org/10.1007/3-540-11913-2_4.

56. Girdzis, S.P., Lin, Y., Leppert, L., Slavney, A.H., Park, S., Chapman, K.W., Karunadasa, H.I., and Mao, W.L. (2021). Revealing local disorder in a silver-bismuth halide perovskite upon compression. J. Phys. Chem. Lett. *12*, 532–536. https://doi.org/10.1021/acs.jpclett.0c03412.

57. Schilcher, M.J., Robinson, P.J., Abramovitch, D.J., Tan, L.Z., Rappe, A.M., Reichman, D.R., and Egger, D.A. (2021). The significance of polarons and dynamic disorder in halide perovskites. ACS Energy Lett. *6*, 2162–2173. https://doi.org/10.1021/acsenergylett.1c00506.

58. Blum, V., Gehrke, R., Hanke, F., Havu, P., Havu, V., Ren, X., Reuter, K., and Scheffler, M. (2009). Ab initio molecular simulations with numeric atom-centered orbitals. Comput. Phys. Commun. *180*, 2175–2196. https://doi.org/10.1016/j.cpc.2009.06.022.

59. Perdew, J.P., Burke, K., and Ernzerhof, M. (1996). Generalized gradient approximation made simple. Phys. Rev. Lett. *77*, 3865–3868. https://doi.org/10.1103/PhysRevLett.77.3865.

60. Tkatchenko, A., and Scheffler, M. (2009). Accurate molecular van der waals interactions from ground-state electron density and free-atom reference data. Phys. Rev. Lett. *102*, 073005. https://doi.org/10.1103/PhysRevLett.102.073005.

61. Kim, Y.-H., Song, R., Hao, J., Zhai, Y., Yan, L., Moot, T., Palmstrom, A.F., Brunecky, R., You, W., Berry, J.J., et al. (2022). The structural origin of chiroptical properties in perovskite nanocrystals with chiral organic ligands. Adv. Funct. Mater. *32*, 2200454. https://doi.org/10.1002/adfm.202200454.

62. Weadock, N.J., MacKeen, C., Qin, X., Waquier, L., Rakita, Y., Vigil, J.A., Karunadasa, H.I., Blum, V., Toney, M.F., and Bridges, F. (2023). Thermal contributions to the local and long-range structural disorder in $CH_3NH_3PbBr_3$. PRX Energy *2*, 033004. https://doi.org/10.1103/PRXEnergy.2.033004.

63. Biliroglu, M., Türe, M., Ghita, A., Kotyrov, M., Qin, X., Seyitliyev, D., Phonthiptokun, N., Abdelsamei, M., Chai, J., Su, R., et al. (2025). Unconventional solitonic high-temperature superfluorescence from perovskites. Nature *642*, 71–77. https://doi.org/10.1038/s41586-025-09030-x.

64. Chakraborty, R., Bobay, B., Qin, X., Blum, V., and Mitzi, D.B. (2026). Local symmetry breaking in 3d hybrid perovskites with 3-hydroxyazetidinium. J. Am. Chem. Soc. *148*, 9720-–9728. https://doi.org/10.1021/jacs.5c21300.

65. Ong, S.P., Richards, W.D., Jain, A., Hautier, G., Kocher, M., Cholia, S., Gunter, D., Chevrier, V.L., Persson, K.A., and Ceder, G. (2013). Python materials genomics (pymatgen): A robust, open-source python library for materials analysis. Comput. Mater. Sci. *68*, 314–319. https://doi.org/10.1016/j.commatsci.2012.10.028.

66. Togo, A., Shinohara, K., and Tanaka, I. (2024). Spglib: a software library for crystal symmetry search. Sci. Technol. Adv. Mater.: Methods *4*, 2384822. https://doi.org/10.1080/27660400.2024.2384822.

67. Togo, A., and Tanaka, I. (2015). First principles phonon calculations in materials science. Scr. Mater. *108*, 1–5. https://doi.org/10.1016/j.scriptamat.2015.07.021.

68. Shang, H., Raimbault, N., Rinke, P., Scheffler, M., Rossi, M., and Carbogno, C. (2018). All-electron, real-space perturbation theory for homogeneous electric fields: theory, implementation, and application within DFT. New J. Phys. *20*, 073040. https://doi.org/10.1088/1367-2630/aace6d.